HEMATOPOIESIS AND STEM CELLS

Adult blood stem cell localization reflects the abundance of reported bone marrow niche cell types and their combinations

Konstantinos D. Kokkaliaris,[1-4] Leo Kunz,[1] Nina Cabezas-Wallscheid,[5-7] Constantina Christodoulou,[4,8] Simon Renders,[5,6] Fernando Camargo,[4,8] Andreas Trumpp,[5,6] David T. Scadden,[2-4] and Timm Schroeder[1]

[1]Department of Biosystems Science and Engineering, Eidgenössische Technische Hochschule (ETH) Zurich, Basel, Switzerland; [2]Center for Regenerative Medicine, Massachusetts General Hospital, Boston, MA; [3]Harvard Stem Cell Institute, Cambridge, MA; [4]Department of Stem Cell and Regenerative Biology, Harvard University, Cambridge, MA; [5]German Cancer Research Center (DKFZ) and DKFZ-Zentrum für Molekulare Biologie der Universität Heidelberg (ZMBH) Alliance, Heidelberg, Germany; [6]Heidelberg Institute for Stem Cell Technology and Experimental Medicine (HI-STEM), Heidelberg, Germany; [7]Max Planck Institute of Immunobiology and Epigenetics, Freiburg, Germany; and [8]Stem Cell Program, Boston Children's Hospital, Boston, MA

KEY POINTS

- **The homeostatic bone marrow localization of femoral and sternal HSCs reflects the abundance of microenvironmental cell types.**

- **Juvenile HSCs show preferential association with Cxcl12 stroma cells.**

The exact localization of hematopoietic stem cells (HSCs) in their native bone marrow (BM) microenvironment remains controversial, because multiple cell types have been reported to physically associate with HSCs. In this study, we comprehensively quantified HSC localization with up to 4 simultaneous (9 total) BM components in 152 full-bone sections from different bone types and 3 HSC reporter lines. We found adult femoral α-catulin-GFP+ or Mds1GFP/+Flt3Cre HSCs proximal to sinusoids, Cxcl12 stroma, megakaryocytes, and different combinations of those populations, but not proximal to bone, adipocyte, periarteriolar, or Schwann cells. Despite microanatomical differences in femurs and sterna, their adult α-catulin-GFP+ HSCs had similar distributions. Importantly, their microenvironmental localizations were not different from those of random dots, reflecting the relative abundance of imaged BM populations rather than active enrichment. Despite their functional heterogeneity, dormant label-retaining (LR) and non-LR hematopoietic stem and progenitor cells both had indistinguishable localization from α-catulin-GFP+ HSCs. In contrast, cycling juvenile BM HSCs preferentially located close to Cxcl12 stroma and farther from sinusoids/megakaryocytes. We expect our study to help resolve existing confusion regarding the exact localization of different HSC types, their physical association with described BM populations, and their tissue-wide combinations. (*Blood*. 2020;136(20):2296-2307)

Introduction

The BM microenvironment is important in controlling hematopoietic stem cell (HSC) fates throughout life.[1-3] Bone marrow (BM) HSCs reside in specialized anatomical microenvironments.[4] To date, HSCs have been reported to physically associate with a plethora of BM components.[3,5,6] Early studies identified the association of HSCs with bone-lining osteoblasts after transplantation,[7-9] whereas homeostatic HSCs have been reported close to nonmyelinated Schwann cells,[10] nestin[11] and Cxcl12-expressing stroma,[12,13] megakaryocytes (MKs),[14-16] BM vasculature,[17] and specific vessels and perivascular cells (arterioles/periarteriolar[18] or sinusoids/perisinusoidal[13]). These data mainly come from studies measuring HSC distances from only a limited number of single BM populations and often in different bone types, resulting in contradictory findings. Thus, the cellular composition of the BM microenvironment surrounding HSCs remains disputed.

The existence of distinct niches supporting different HSC subtypes also continues to be debated. Arteriolar and NG2+

periarteriolar cells were described as preferential niches for quiescent Ki67-HSCs,[18] whereas another study reported no difference in localization of quiescent and cycling HSCs relative to arterioles, sinusoids, or transition zone vessels.[13] Although most HSCs are quiescent at individual time points, only a few show long-term quiescence (dormancy).[19] Those rare HSCs contain the highest regeneration potential after transplantation, and can be identified by long-term retention of fluorescent biomarkers (label-retaining; LR), whereas their dividing counterparts gradually dilute and lose fluorescence and repopulation potential (non-LR).[19,20] A limited number of mouse models enables endogenous labeling of hematopoietic stem and progenitor cells (HSPCs).[19,21] Visualizing genetically labeled LR and non-LR HSPCs in situ has been challenging, mainly because of their low frequency and need for quantitative BM imaging for their accurate classification.

Cell-cycle properties of HSCs are age dependent. BM HSCs retain fetal liver characteristics (active cycling) for the first 3 weeks after birth.[22] A few days later, they switch to an adult

phenotype showing the divisional properties and repopulation kinetics of adult HSCs. Whether pre- and postswitch HSCs occupy distinct niches is currently unclear.

To resolve existing uncertainties regarding HSC localization and better quantify the complexity of their 3-dimensional (3D) microenvironment, we used novel quantitative multicolor imaging of thick full-bone sections,[23] in different bone types and developmental stages. To maximize the number of simultaneously imaged BM populations, we used 3 different reporter mouse systems that allowed for efficient 2-marker detection of HSCs/HSPCs (c-Kit and α-catulin-GFP+,[13] c-Kit and Mds1GFP/+Flt3Cre,[24] and c-Kit and doxycycline [DOX]-treated SCL/tTA;H2B-GFP[19] mice). We comprehensively quantified HSC localization in relation to up to 4 simultaneous (9 total) BM components and their combinations at the tissue-wide level with single-cell resolution.

Methods

Mice

Mice were bred under specific pathogen-free conditions, and all procedures were approved by the cantonal veterinary office of Basel-Stadt, Switzerland; German authorities; and the Institutional Animal Care and Use Committee of Massachusetts General Hospital. For HSC identification, we used α-catulinGFP/+ and Mds1GFP/+Flt3Cre knockin lines[13,24] or double-transgenic SCL-tTA;H2B-GFP animals treated with DOX for 150 days, as previously described.[19] To reliably identify dormant label-retaining HSPCs, we compared BM sections from age-matched controls and treated mice immunostained in parallel and imaged sequentially with the same microscope and same settings. Cxcl12tm2.1Sjm/J mice were used for detection of Cxcl12-producing cells.[25]

Bone sectioning and immunostaining

Bones were processed as previously described.[23] Supplemental Table 1, available on the *Blood* Web site, lists all antibodies used in the study. Optically cleared (2,2-thiodiethanol; Sigma-Aldrich) sections were mounted using 100% 2,2-thiodiethanol with 0.1 M *N*-propyl gallate (pH 8.5; refractive index = 1.518; Sigma-Aldrich) in silicon spacers (Grace Biolabs) and 0.13- to 0.16-mm-thick coverslips (No. 1; Ted Pella).

Confocal microscopy

Confocal imaging was performed with a Leica TCS SP8 microscope equipped with 3 photomultiplier tubes, 2 HyD detectors, and 5 laser lines: 405-nm blue diode, argon (458, 476, 488, 496, and 514 nm), and 3 helium neon (543, 594, and 633 nm). All imaging was performed with type F immersion liquid (Leica) matching the refractive index of our optically cleared sections to avoid mismatches, and a 20× multi-immersion objective (numerical aperture, 0.75; free working distance, 0.680 mm) at 400-Hz, bidirectional mode with 2.49 z-spacing. Eight-bit images were acquired with 0.85 zoom at 1024 × 1024 resolution. Optimal settings (laser power, detector bandwidth, gain, and offset) were based on fluorescence minus one (FMO) controls.

Analysis

Image analysis was performed with Imaris ver. 8.3.1, 9.1.2, or 9.5.1 (Bitplane) using the MeasurementPro and ImarisXT extensions. Distance transformations were performed in 16-bit transiently converted data to avoid truncation. To identify individual HSCs (cKit+α-catulin-GFP+), we first segmented cKit+

cells with the Imaris surface function (split touching objects), to distinguish cKit+ hematopoietic cells from BM endothelium (α-catulin-GFP+cKit−). cKit+ cells were separated based on GFP expression and filtered for cKit+ α-catulin-GFP+ objects (mean fluorescence intensity [MFI] of GFP above background based on FMO controls). Finally, we visually inspected all gated objects to confirm their immunophenotype (α-catulin-GFP+cKit+ double positive), size, morphology (small, round cells), and correct signal localization (homogenous GFP signal throughout the cell and membrane cKit staining). Only cKit+GFP+ objects/cells fulfilling all 4 criteria were classified as HSCα-cats, HSCMFGs, or LR/non-LR HSPCs (examples of excluded objects in supplemental Figure 2B). BM populations were segmented using the Imaris surface function, and individual structures were curated based on morphological features. To confine the NG2 signal to pericytes associated with arteries and exclude it from osteoblasts,[26] we computationally masked NG2 signal inside the bone isosurface (masked with collagen 1 [col.1]/osteopontin [opn]) and away from Sca1+ arteries/arterioles to appear black. Random dots (RDs) were generated as described.[23] RDs located inside vessels or bone structures were removed by Imaris. Final BM volume was defined by the less deep fluorescent channel. A self-written script was developed to enable calculation of available combinations of BM locations in full-bone sections (detailed description in supplemental Material).

Statistical analysis

Results were analyzed with GraphPad Prism, using the Kolmogorov-Smirnov test for distributions and the unpaired, nonparametric 2-tailed Mann-Whitney *U* test to compare individual bins unless otherwise stated in the figure legends (including the number of replicates and *P* values).

Code availability

The open-source software used for random dot generation is available at https://www.bsse.ethz.ch/csd/software/XiT.html.

Results

Multicolor imaging allows for simultaneous visualization of HSCs and multiple BM niche components

Our multicolor deep-tissue–imaging pipeline allows for simultaneous visualization of HSCs and up to 4 BM components in full-bone sections of different bones (Figure 1A-B; supplemental Figure 1; Video 1). To efficiently identify HSCs in situ, we used α-catulinGFP/+ mice expressing GFP from the *Ctnnal1* promoter active in HSCs and BM endothelial cells.[13] Detecting homogenous GFP signal surrounded by cKit cell-surface expression in small cells with round morphology enabled 2-color HSC identification (HSCα-cat), with purity comparable to the more complex marker combinations[13] (supplemental Figure 2A-C). Furthermore, we imaged the recently established HSC reporter mouse Mds1GFP/+Flt3Cre (MFG) in which GFP expression is restricted in primitive HSCs (HSCMFGs).[24] Combining all those criteria (immunophenotype, signal localization, cell size, and morphology), we examined >3.5 × 10^6 cKit+ cells with detectable GFP signal and visually confirmed 4067 HSCα-cats and 1336 HSCMFGs in 115 full-bone sections (see "Methods" for more details).
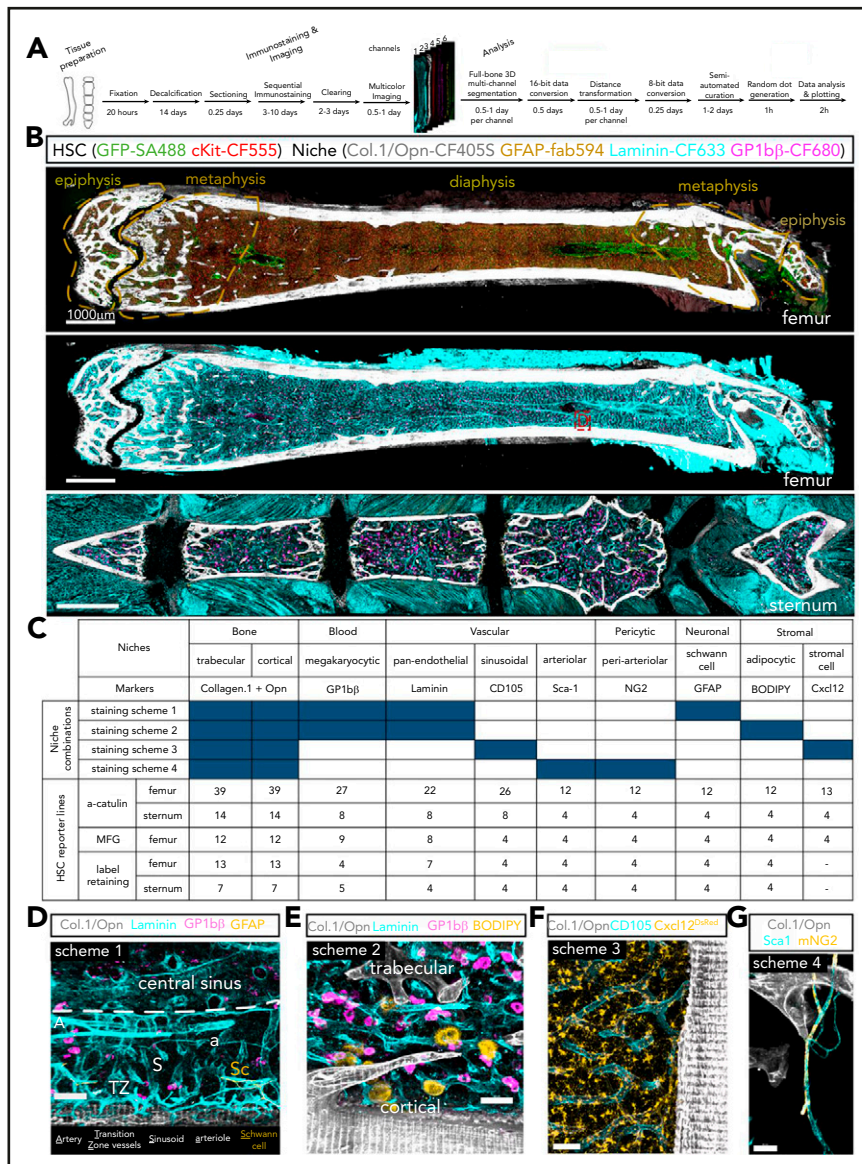
Figure 1. Multicolor simultaneous full-bone quantitative imaging of HSCs and multiple niche populations. (A) Experimental flow and duration of large-volume, multicolor, quantitative confocal imaging. See description in "Analysis" in "Methods." (B) Six-color immunostaining of 220- to 250-μm–thick, full-bone, longitudinal sections of mouse femur (top) and sternum (bottom) from an α-catulin[GFP/+] reporter mouse. Sections stained for collagen.1/osteopontin-CF405S (trabecular and cortical bone), GFAP fab-Alexa-594 (nonmyelinated Schwann cells), laminin-CF633 (vasculature), and GP1bβ-CF680 (MKs). HSC[α-cat]s were marked by GFP (amplified by biotin-streptavidin 488) and cKit-CF555 expression. CF, cyanine-based fluorescent dyes, SA, streptavidin. (C) Overview of niche components, respective marker combinations, and staining schemes. The number of sections imaged for each niche population, marker, bone type, and HSC reporter system are shown. (D-G) High-magnification images of multicolor staining schemes for niche components. (D) Femoral area (enlargement of red dashed square appearing in panel B) showing nonmyelinated Schwann cells (Sc, yellow, GFAP); cortical bone (white, Col.1/Opn); MKs (magenta, GP1bβ); and different vessel types marked by laminin: central sinus, sinusoids (S), arteries (A), arterioles (a) and transition zone vessels (TZ). (E) Trabecular and cortical bone (white, Col.1/Opn), adipocytes (yellow; boron dipyrromethene, BODIPY TRx), and BM vasculature (cyan, laminin). (F) Cortical bone (white, Col.1/Opn), sinusoids (cyan, CD105), and Cxcl12+ stroma (yellow). (G) Trabecular bone (white, Col.1/Opn), Sca1+ arteries (cyan), and NG2+ periarteriolar cells (yellow) after computationally masking all NG2+ objects outside Sca1+ arteriolar signal to appear black. Scale bars: 1000 μm (B), 100 μm (D), 50 μm (E, G), and 30 μm (F).

We established multicolor stainings for 9 distinct BM components (Figure 1C; supplemental Table 1). We used antibody stainings and morphological features to identify cortical and trabecular osteoblasts and bone matrix (Col.1/Opn), MKs (glycoprotein Ibβ [GP1bβ]), the entire vasculature (laminin) and distinct vessel types (CD105 for sinusoidal and Sca1 for arteriolar cells), periarteriolar cells (neuronal/glial antigen 2 [NG2]), adipocytes (BODIPY), stromal cells (Cxcl12-DsRed mouse),[25] and nonmyelinated Schwann cells (glial fibrillary acidic protein [GFAP]; Figure 1D-G).

Localization of adult HSCs in relation to individual BM populations is conserved in different HSC reporters and bone types

To identify BM populations associated with HSC[α-cat]s, we first quantified the distance of every HSC[α-cat] from individual BM components in full-bone sections (Figure 2). In the femurs, HSC[α-cat]s were scattered throughout the BM as single cells, mostly locating in the diaphysis around the central sinus, which occupies a large percentage of the BM diaphyseal space in long bones (supplemental Figure 2D-H). We did not observe clusters, as most HSC[α-cat]s were >40 μm away from their closest HSC neighbor (supplemental Figure 2D). To assess whether this HSC localization reflects the abundance of different BM populations, RDs of HSC size were computationally placed throughout the BM volume, excluding the insides of the bone matrix and blood vessels. Because the depth of detection varies between different fluorescent channels, depending on fluorochrome, excitation laser, and the epitope's density, only those RDs located within the 3D volume defined by the shallowest marker fluorochrome were analyzed.[23] This method was crucial for unbiased statistical analysis, because placing RDs in the entire imaging volume leads to noncomparable spatial distributions of RDs vs cells and wrong conclusions (supplemental Figure 2E).

Most HSCs were not close to trabecular and cortical bone, adipocytes, or nonmyelinated Schwann cells; rather, they were >90 μm away (Figure 2B-D; supplemental Figure 3). Instead, a proportion of HSC[α-cat]s were close to MKs, and most were in proximity to the Cxcl12 stroma and vasculature. Importantly, none of these
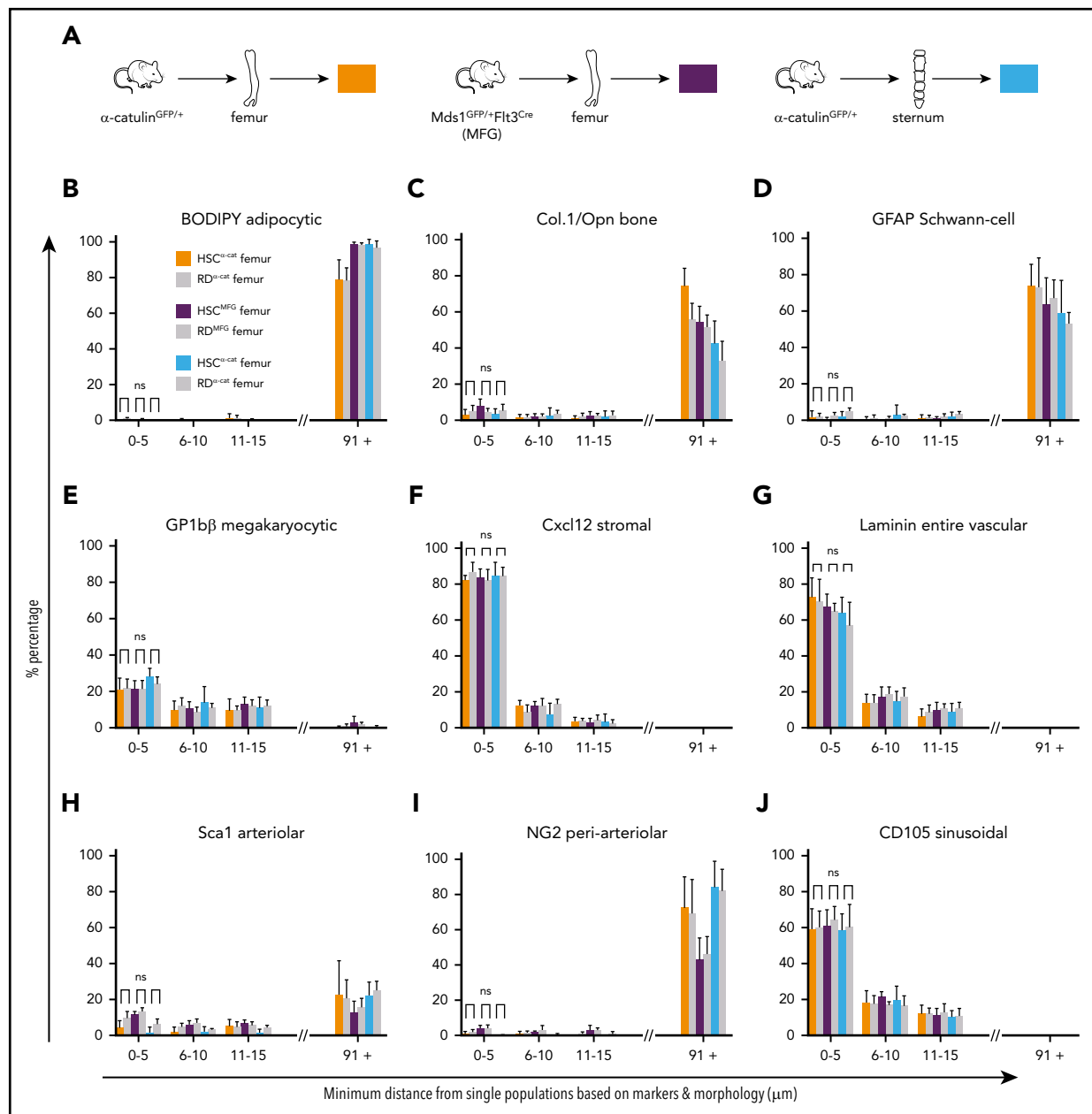
**Figure 2. Despite anatomical differences, femoral and sternal HSC$^{α\text{-cat}}$s and femoral HSC^{MFG}s mainly associate with sinusoids and Cxcl12 stroma cells, reflecting frequencies of imaged BM.** (A) Overview of HSC reporter mouse lines and corresponding bones used for full-bone, multicolor, quantitative imaging and analysis. (B-J) HSC-niche distance quantification in femurs and sterna of α-catulin$^{GFP/+}$ and Mds1$^{GFP/+}$Flt3^{Cre} reporter mice. (B-D) BODIPY$^+$ adipocytes (B; n = 4 each); Col.1$^+$/Opn$^+$ bone surfaces (C; α-catulin$^{GFP/+}$ femur, n = 13; Mds1$^{GFP/+}$Flt3^{Cre} femur, n = 12; α-catulin$^{GFP/+}$ sternum, n = 14); and GFAP$^+$ Schwann cells (D; n = 4 each) were not associated with HSC$^{α\text{-cat}}$s. (E-G) Both femoral and sternal HSC$^{α\text{-cat}}$s randomly associated with GP1bβ MKs (E; α-catulin$^{GFP/+}$ femur, n = 12; Mds1$^{GFP/+}$Flt3^{Cre} femur, n = 9; α-catulin$^{GFP/+}$ sternum, n = 8); Cxcl12 stroma (F; α-catulin$^{GFP/+}$ femur, n = 5; Mds1$^{GFP/+}$Flt3^{Cre} femur and α-catulin$^{GFP/+}$ sternum, n = 4); and laminin$^+$ entire BM vasculature (F-G; α-catulin$^{GFP/+}$ femur, n = 9; Mds1$^{GFP/+}$Flt3^{Cre} femur and α-catulin$^{GFP/+}$ sternum, n = 8). (H-J) Only a minority of femoral and sternal HSC$^{α\text{-cat}}$s localized near Sca1$^+$ arteriolar (H; n = 4 each) and NG2$^+$ periarteriolar niches (I; n = 4 each), whereas most were randomly associated with CD105$^+$ sinusoids (J; α-catulin$^{GFP/+}$ femur, n = 12; Mds1$^{GFP/+}$Flt3^{Cre} femur, n = 4; α-catulin$^{GFP/+}$ sternum, n = 8). Data in panels B-J represent mean ± standard deviation. Statistical significance for the 0- to 5-μm bin was assessed by 2-tailed nonparametric Mann-Whitney U test. *$P < .05$; **$P < .01$; ***$P < .001$.

relationships were significantly different from RD localization (Figure 2E-G). HSCs were distant from Sca1$^+$ arteriolar and NG2$^+$ periarteriolar cells, but close to CD105$^+$ sinusoids (Figure 2H-J; supplemental Figure 3G-I). Only a small proportion of femoral HSC$^{α\text{-cat}}$s were adjacent to Sca1$^+$ arteriolar and NG2$^+$ periarteriolar cells (6% ± 3% and 1% ± 2%, respectively), whereas 80% located >20 μm away. The percentage of HSC$^{α\text{-cat}}$s found close to BM populations and their distance distribution were similar to that of the RDs in all cases, indicating that femoral HSC$^{α\text{-cat}}$s were close to MKs, Cxcl12 stroma, and sinusoids because of the high frequency of those cell types rather than as the result of active enrichment. Similar results were obtained in MFG mice, where the localization of cKit$^+$GFP$^+$ HSC^{MFG}s, including the frequency of those within 5 μm of individual BM populations, was also indistinguishable from RDs (Figure 2). Notably, individual HSCs can be found close to any cell type, if assessed in small-volume BM
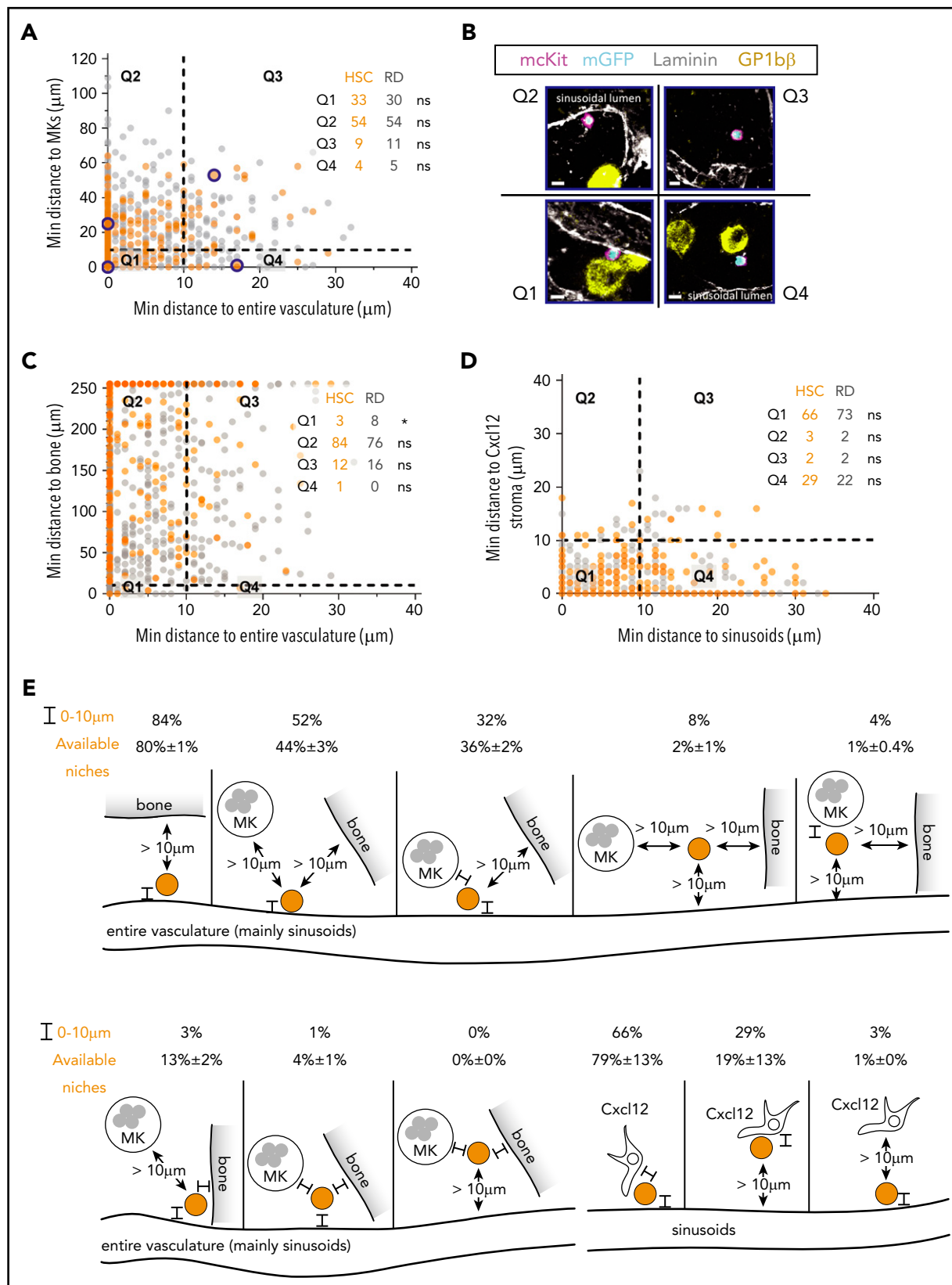
Figure 3. HSC$^{\alpha\text{-cat}}$s occupy different BM locations composed of discrete cell types. (A-D) Quantification of HSC$^{\alpha\text{-cat}}$ localization in relation to combinatorial BM niches. Scatterplot showing 2-dimensional [2D] distance quantification of single HSCs in relation to the entire vasculature and MKs (A) and the corresponding high-magnification images (B) or entire vasculature and bone (C). Most HSC$^{\alpha\text{-cat}}$s located proximal to the vasculature (A; Q2 and Q1) and did not simultaneously associate with MKs (A; Q2 vs Q1); almost all HSC$^{\alpha\text{-cat}}$s found close to MKs (A; Q1 and Q4) were also close to the vasculature (A; Q1 vs Q4). Dots represent 261 individual HSCs (orange; n = 6) and 584 RDs (gray; n = 6). Data points highlighted with blue circles are shown in panel B. To highlight the cells of interest in panel B (cKit$^+$GFP$^+$ cell), cKit and GFP signal outside the cells were computationally

snapshots. However, quantifying many HSCs throughout thick full-bone sections elucidates that some relationships are only infrequent. Therefore deep, large-volume, full-bone quantitative imaging is indispensable for accurate assessment of HSC localization.

To investigate whether reported controversies in HSC localization[13,18] stem from different types of bones imaged previously, we extended our study to the mouse sternum. Anatomically, the sternum consists of individual bone segments that lack central diaphyseal areas of long bones, but are rich in trabecular bone areas, similar to the femoral epi-/metaphysis (Figure 1B). Despite the microanatomical differences, HSC$^{\alpha\text{-cat}}$s physically associated with the same BM populations in femurs and sterna (Figure 2; supplemental Figure 4). A marginally higher proportion of sternal HSC$^{\alpha\text{-cat}}$s located close to MKs, but so did the RDs (Figure 2E).

HSCs reside in complex combinatorial microenvironments reflecting cellular abundance of BM populations

To better dissect the HSC microenvironment complexity, we quantified HSC$^{\alpha\text{-cat}}$ localization in relation to combinations of up to 4 BM components simultaneously. Most of the HSC$^{\alpha\text{-cat}}$s located within 10 μm (~1 HSC diameter) from vasculature. Simultaneous quantification of distance from MKs revealed that most of those HSC$^{\alpha\text{-cat}}$s were >10 μm away from the MKs, whereas some were close to both (Figure 3A-B; Q2 vs Q1). Conversely, of the 1 in 3 HSC$^{\alpha\text{-cat}}$s locating within 10 μm of the MKs, almost all were also close to the vasculature. Only a small proportion of HSC$^{\alpha\text{-cat}}$s located within 10 μm of the bone. Consistent with bone surface vascularization[13] almost all of those are also proximal to the vasculature (Figure 3C; Q1 vs Q4). Interestingly, 66% of HSC$^{\alpha\text{-cat}}$s located within 10 μm of both sinusoids and Cxcl12 stroma, whereas 29% were close only to Cxcl12 stroma (Figure 3D; Q1 and Q4), showing that HSC$^{\alpha\text{-cat}}$s did not homogenously associate with 1 or a combination of BM populations, but occupied multiple combinatorial BM environments composed of vasculature and/or MKs or sinusoids and/or Cxcl12 stroma (Figure 3E; supplemental Figure 5).

Quantification of the absolute number of available BM locations and their HSC occupancy further confirmed these conclusions. We computationally calculated the number of all available 3-dimensional BM locations composed of different combinations of BM components within which a single HSC could physically fit (3D areas of a 10-μm diameter; see supplemental Methods for details). Per full-femur section, we estimated an average of 114 521 (79%) locations close to both sinusoids and Cxcl12$^+$ stroma, 27 641 (19%) close to Cxcl12 stroma only, 1 213 (<1%) close to sinusoids only, and 435 (<1%) close to neither. The frequencies of these 4 BM locations (79% vs 19% vs <1% vs <1%, respectively) resembled the frequencies of HSCs found close to them (Figure 3E). The same holds true when quantifying BM locations consisting of 3 populations: entire vasculature, bone, and/or MKs (Figure 3E). This result confirmed that the proximity of HSCs to specific BM populations was governed by the abundance of these cell types and did not reflect active enrichment

of the populations imaged here. In addition, available absolute numbers of those BM locations were not limiting, given that only 0.03% were occupied by HSCs. Our data provide quantitative evidence that HSC localization within the BM microenvironments reflects the abundance of those microenvironment populations.

Quantitative imaging enables reliable identification of endogenously labeled dormant LR and non-LR adult HSPCs in situ

To investigate whether those complex BM locations host different HSC subtypes, we quantified the location of dormant and non-dormant adult HSPCs. We used double-transgenic SCL-tTA;H2B-GFP mice treated with DOX for 150 days and aged-matched SCL-tTA and H2B-GFP single transgenic animals as controls (Figure 4A-C). This system enabled DOX-dependent labeling of homeostatic HSPCs with histone H2B-GFP.[19] When DOX was administered (chase period), H2B-GFP transcription stopped, resulting in progressive GFP dilution in HSPCs with a history of proliferation (non-LR), whereas dormant HSPCs retained their fluorescence (LR; Figure 4C-D). Dormant LR HSPCs contain most of the transplanted stem cell activity, whereas non-LR cells mainly have limited self-renewing capacity.[19] Because hematopoietic progenitors divide more frequently than HSCs, the 150-day-long chase period ensured HSC-specific labeling (Figure 4E).[27]

As expected, the GFP MFI of cKit$^+$ cells in SCL-tTA control mice was at background levels. H2B-GFP mice (without tTa expression) showed low but detectable leaky fluorescence (Figure 4D). DOX-treated SCL-tTA;H2B-GFP mice displayed a range of GFP intensities, including those higher than H2B-GFP controls. We used the maximum GFP intensity of cKit$^+$GFP$^+$ cells from age-matched H2B-GFP controls as the threshold,[28] above which cells were classified as LR (Figure 4F). Notably, the number of LR HSPCs per full-bone section was twofold lower than in the HSC$^{\alpha\text{-cat}}$s. The remaining cKit$^+$GFP$^+$ cells were classified as non-LR and were considered nondormant HSPCs with a history of proliferation.[19-21] Digital GFP quantification was essential for accurate distinction between LR and non-LR HSPCs, because visual decision could lead to misclassification (Figure 4G). Our approach enabled in situ identification of endogenously labeled dormant and nondormant HSPCs in the same section (Figure 4H).

Dormant and nondormant adult HSPCs and HSC$^{\alpha\text{-cat}}$s have indistinguishable BM localization

To address whether dormant LR and nondormant, non-LR HSPCs are associated with distinct BM microenvironments, we quantified their BM localization. Consistent with our HSC$^{\alpha\text{-cat}}$ data, LR and non-LR HSPCs did not locate near adipocytes, bone surfaces, or nonmyelinated Schwann cells, with <5% being within 5 μm of these structures and most being >90 μm away (Figure 5A-C). Although few LR and non-LR cells located close to the MKs, most were close to the BM vasculature, similar to RDs and HSC$^{\alpha\text{-cat}}$s (Figure 5D-E). Distance quantification from distinct vessels and pericytes revealed that only a small fraction of LR and non-LR HSPCs were close to Sca1$^+$ arteries and NG2 periarteriolar cells, similar to RDs (Figure 5F-G). Instead, almost 60% of LR and non-LR cells located >50 μm from Sca1$^+$ arteries
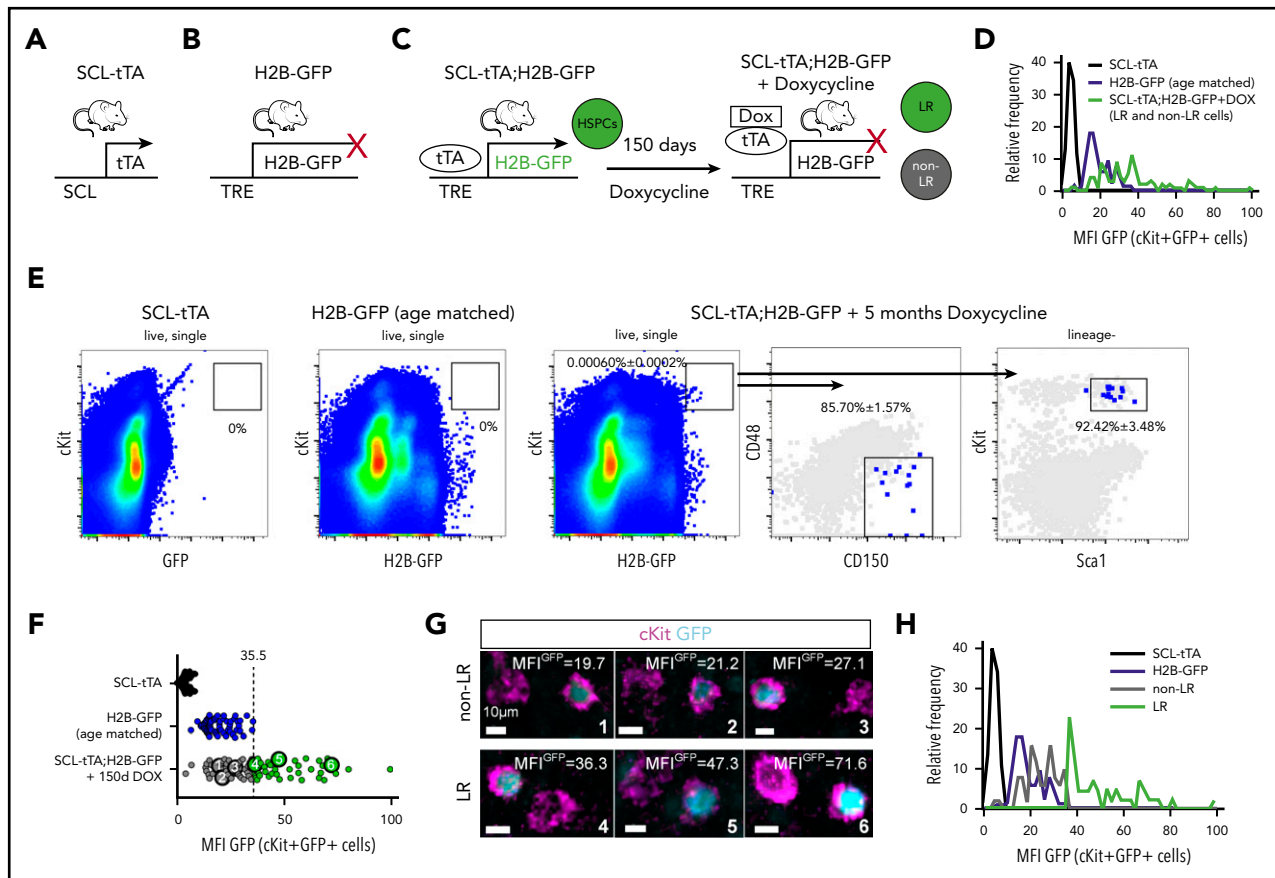
Figure 4. Identification of dormant label-retaining and nondormant HSPCs in situ by quantitative BM imaging. (A-C) Representation of the experimental approach for endogenous labeling of dormant LR HSPCs. Transgenic mice expressing tetracycline transactivator in HSPCs from the scl gene locus (A; SCL-tTA) and the histone 2B-GFP fusion protein (H2B-GFP) under the control of the tetracycline-responsive regulatory element (B; TRE; H2B-GFP) were crossed to confine GFP expression to the HSPCs (C, left; SCL-tTA; H2B-GFP). In the presence of DOX, H2B-GFP transcription was inhibited, resulting in dilution of GFP signal by proliferating cells. (D-G) Identification of BM LR and non-LR HSPCs in situ by quantitative imaging. (D) Frequency distribution of GFP levels (MFI) of cKit[+]GFP[+] (see "Methods" for identification criteria) cells from imaging of SCL-tTA (110 cells), H2B-GFP control (67 cells), and DOX-treated SCL-tTA;H2B-GFP mice (96 cells). (E) Flow cytometry of SCL-tTA, H2B-GFP, and double transgenic SCL-tTA;H2B-GFP mice treated for 150 days with DOX revealed the high purity of HSC marker expression in cKit[+]GFP^{high} LR cells (n = 3). (F) Dot plot showing the absolute GFP MFI (MFI[GFP]) of cKit[+]GFP^{+} single cells from control and treated mice shown in panel D (SCL-tTA: MGI[GFP] = 4.8; H2B-GFP: MGI[GFP] = 19.2; DOX-treated SCL-tTA;H2B-GFP: MGI[GFP] = 35.99). Note the leakiness of GFP expression in the cKit[+]GFP^{+} BM cells of the H2B-GFP mouse. LR HSPC identification therefore required precise GFP quantification. LR HSPCs were identified as cKit^{+} cells with higher MFI[GFP] than background levels in the single H2B-GFP mouse line (H2B-GFP: maximum MGI[GFP] = 35.3). (G) High-resolution images of BM LR and non-LR HSPCs, illustrating the need for computational quantification. (H) Frequency distribution of LR and non-LR HSPCs after thresholding based on H2B-GFP background fluorescence from aged-matched animals.

(supplemental Figure 6F) and most were >90 μm away from NG2 periarteriolar cells (Figure 5G). In contrast, >60% of LR and non-LR HSPCs located within 5 μm of the CD105^{+} sinusoids (RD, 59% ± 6%; Figure 5H). Importantly, the percentage of femoral LR and non-LR HSPCs found close to individual BM populations and their distance distribution was statistically indistinguishable (Figure 5A-I; supplemental Figure 6). This result was further confirmed by quantifying their proximity to dual BM microenvironments (Figure 5I-J). Similar to HSC[α-cat]s, the localization of LR and non-LR HSPCs was conserved between femurs and sterna (supplemental Figure 7). Thus, dormant LR and nondormant non-LR HSPCs were associated with the same imaged BM populations and had statistically indistinguishable localizations as HSC[α-cat]s in both femurs and sterna.

## Distinct BM localization signature between juvenile and postswitch HSCs

Because dormant and nondormant HSPCs share the same localization in adult animals, we next investigated the BM localization of juvenile 3-week-old HSCs retaining fetal liver characteristics (high proliferation rates) and compared them with postswitch (5-week-old) and adult (12-week-old) HSCs in α-catulin[GFP/+] mice. The BM localization of postswitch 5-week-old and adult 12-week-old HSC[α-cat]s was largely identical, except that 5-week-old HSC[α-cat]s preferentially located close to Cxcl12 stroma (Figure 6A-E; supplemental Figure 8A-E). Comparing pre- and postswitch HSC[α-cat]s, we found no difference in their localization relative to adipocytes, Schwann cells, BM vasculature, and Sca1 arteriolar and NG2 periarteriolar cells (supplemental Figures 8A-E, 9, and 10). However, significantly fewer preswitch HSC[α-cat]s were located close to MKs, a twofold decrease compared with postswitch HSC[α-cat]s (Figure 6B). Similarly, significantly fewer preswitch HSC[α-cat]s located proximal to CD105 sinusoids compared with RDs and postswitch HSC[α-cat]s (Figure 6C). Instead, preswitch HSC[α-cat]s preferentially located close to Cxcl12 stroma irrespective of the distance bin applied and exhibited a marginally higher preference toward bone surfaces, shared equally between trabecular and cortical bone (Figure 6D-F; supplemental Figure 8F-G). We next evaluated whether observed differences
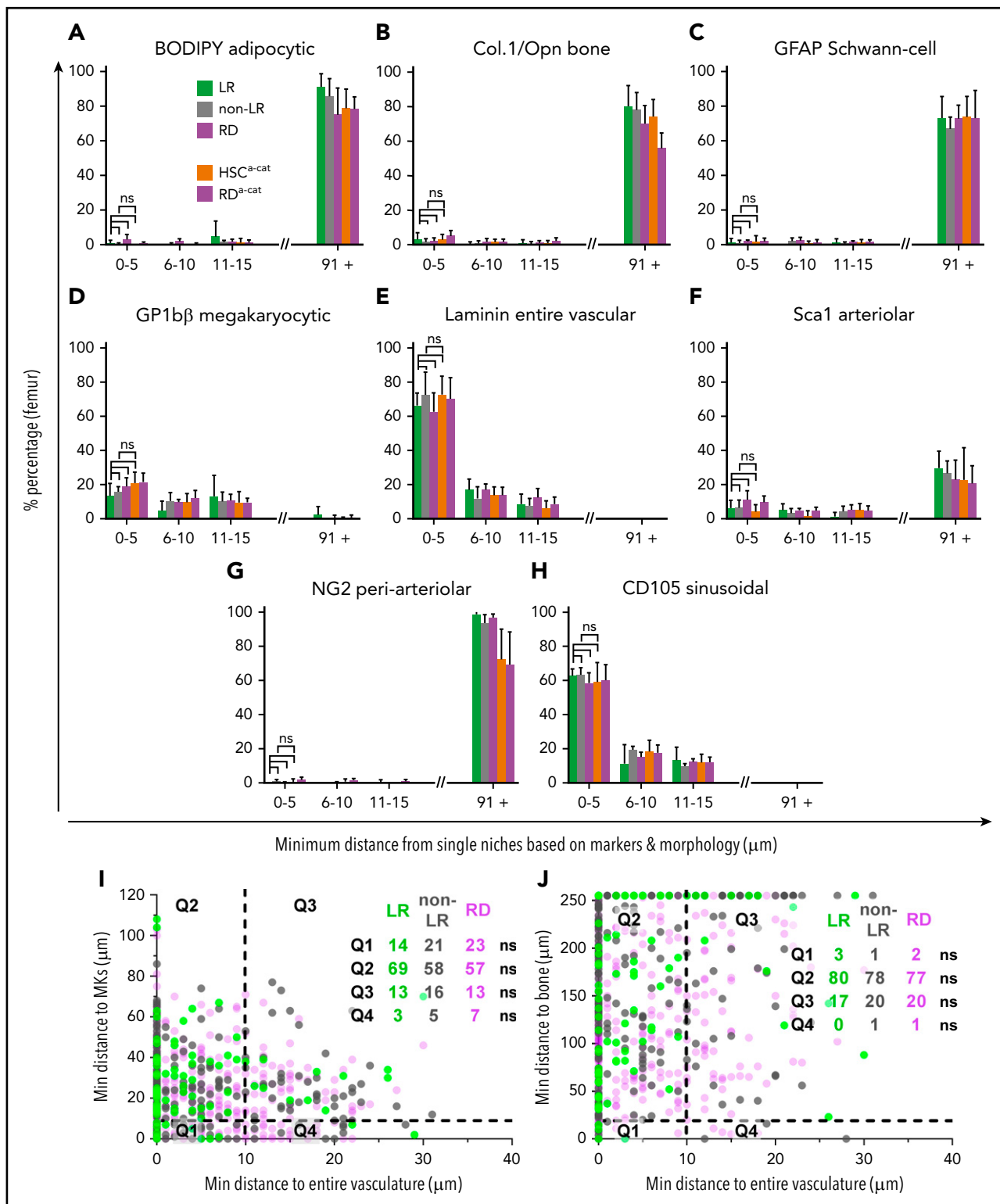
Figure 5. HSC^{α-cat}s, dormant LR HSCs, and nondormant non-LR HSPCs all have similar BM niche signatures. (A-H) Comparative niche distance quantification of LR and non-LR HSPCs in femurs of DOX-treated SCL-tTA;H2B-GFP mice or of HSC$^{α-cat}$s in α-catulin$^{GFP/+}$ reporter mice. (A-C) BODIPY^{+} adipocytes (A; n = 4 each); Col.1^{+}/Opn^{+} bone surfaces (B; n = 13 each); and GFAP^{+} Schwann cells (C; n = 4 each) were not physically associated with HSPCs. (D-G) Some LR, non-LR HSPCs and HSC$^{α-cat}$s located randomly near MKs (D; LR/non-LR, n = 4; HSC$^{α-cat}$, n = 12). Most were randomly associated with laminin^{+} vasculature (E; LR/non-LR, n = 7; HSC$^{α-cat}$, n = 9), whereas a few associated with Sca1^{+} arteries and arterioles (F; n = 4 each) or periarteriolar niches (G; n = 4 each). (H) LR and non-LR HSPCs, as well as HSC$^{α-cat}$s randomly associated with CD105^{+} sinusoids (H; LR/non-LRC, n = 4; HSC$^{α-cat}$, n = 12). (I, J) Scatterplots showing 2-dimentional distance quantification of single LR HSPCs (green), non-LR HSPCs (gray dots), and RDs (purple dots) in relation to the entire vasculature and MKs (I; 90 LR, 270 non-LR and 383 RDs) or bone (J; 90 LR, 270 non-LR and 383 RDs). Data in panels A-H represent mean ± standard deviation. Statistical significance in the 0- to 5-μm bin was assessed by 2-tailed nonparametric Mann-Whitney *U* test. ns, not significant.
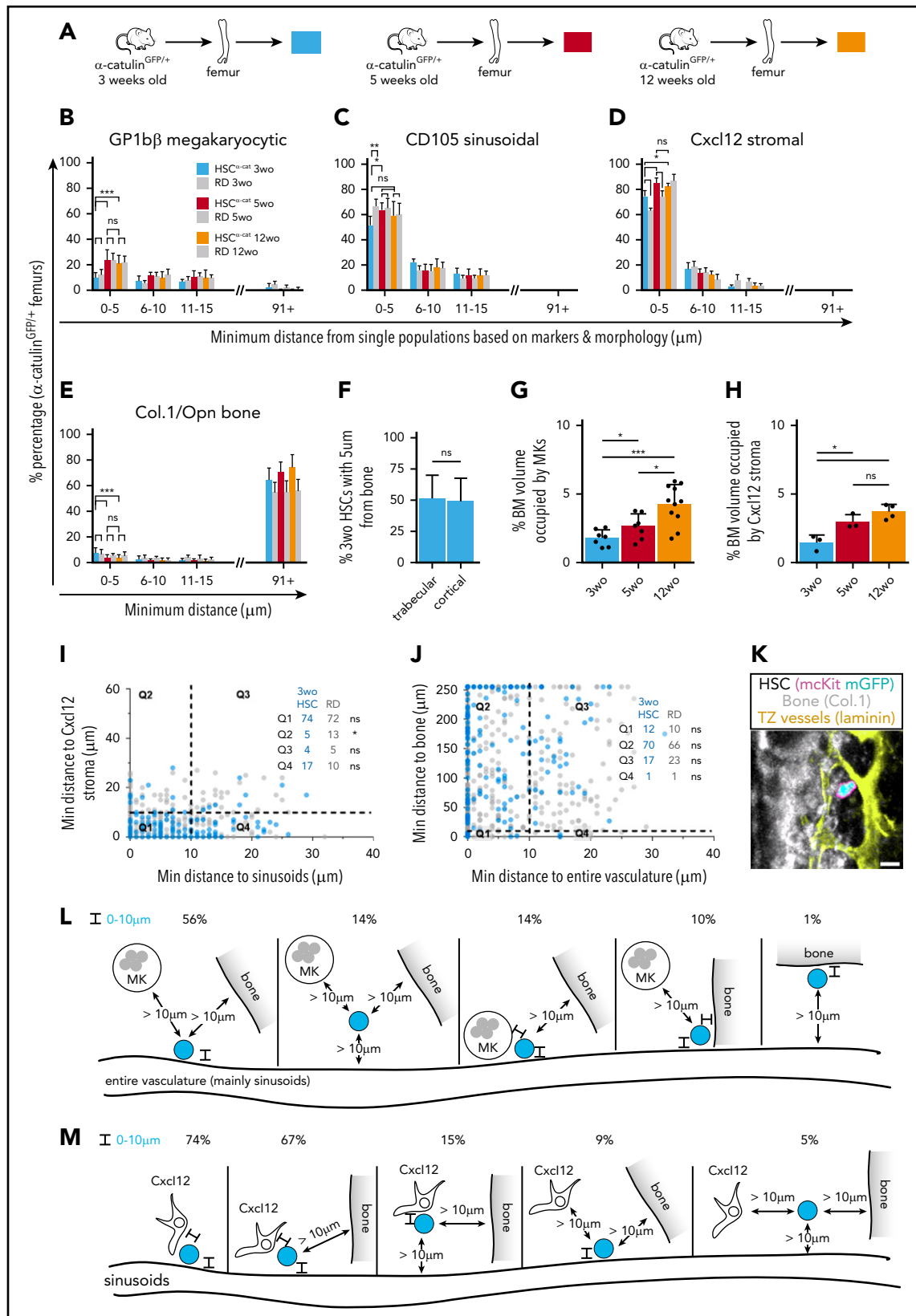
Figure 6. Distinct niche signatures between 3-week-old preswitch and 5- and 12-week-old postswitch HSC$^{\alpha\text{-cat}}$s. (A) Representation of the age groups used for isolation of α-catulin$^{GFP/+}$ femurs. (B-E) Three-week-old (wo) HSC$^{\alpha\text{-cat}}$s were less associated with MKs (B; 3 wo, n = 8; 5 wo, n = 7; 12 wo, n = 12) and CD105$^+$ sinusoids (C; 3 wo, n = 8; 5 wo, n = 6; 12 wo, n = 12), compared with postswitch HSC$^{\alpha\text{-cat}}$s, but were preferentially associated with Cxcl12 stroma (D; 3 wo, n = 4; 5 wo, n = 4; 12 wo, n = 5) and showed a marginally higher preference toward Col.1/Opn$^+$ osteoblasts and bone matrix (E; 3 wo, n = 17; 5 wo, n = 10; 12 wo, n = 13). (F) Percentage of 3-wo HSC$^{\alpha\text{-cat}}$s found within 5 μm of the trabecular or cortical bone surfaces (n = 12). (G-H) Comparison of BM volume occupied by MKs (G; 3 wo, n = 7; 5 wo, n = 7; 12 wo, n = 11) and Cxcl12 stroma (H; 3 wo, n = 3; 5 wo,

between pre- and postswitch HSC$^{\alpha\text{-cat}}$ localization reflected age-related alterations in BM composition and cell abundance. We quantified the BM volume occupied by MKs and Cxcl12 stroma and indeed found a gradual increase with age (Figure 6G-H) that was most likely linked with bone growth (supplemental Figure 8H). Combinatorial localization analysis revealed that significantly fewer preswitch HSC$^{\alpha\text{-cat}}$s were distant from Cxcl12 stroma and close to sinusoids compared with RDs (Q2; Figure 6I). In addition, preswitch HSC$^{\alpha\text{-cat}}$s residing proximal to bone surfaces were also proximal to endosteal vessels (Figure 6J-K), showing that bone surfaces hosting HSCs are vascularized. Thus, most juvenile and adult HSCs associated with sinusoids and Cxcl12 stroma. However, in contrast to adult HSCs, preswitch HSCs were significantly nonrandomly enriched within 5 μm of Cxcl12$^+$ stoma or bone surfaces, and 6 to 15 μm away from CD105 sinusoids. A detailed representation of the distinct BM populations occupied by 3-week-old HSC$^{\alpha\text{-cat}}$s is shown in Figure 6L-M. Taking all evidence together, we report, for the first time to our knowledge, that pre- and postswitch HSCs not only have distinct intrinsic programs, but also have distinct localization in relation to imaged BM populations.

Discussion

Our study contributes to resolving existing confusion regarding exact HSC localization in relation to 9 BM components and their combinations, previously described to function as HSC niches, using quantitative multicolor imaging in 152 full-bone sections from 3 different HSC reporter mouse lines. We have provided a comprehensive data set quantifying the frequencies of HSCs found in close association with those BM populations (supplemental Figure 11). Fourteen percent of our data agree with previous reports, 4% differ, and 82% present novel findings. We showed that HSCs locate within multiple, spatially distinct BM microenvironments mainly composed of sinusoids and Cxcl12 stroma (Figure 3E). The need for physical interaction between HSCs and those cells was supported molecularly, because endothelial and Cxcl12 or LepR perisinusoidal stromal cells are the main sources of stem cell factor, a key protein promoting HSC maintenance.[29,30] To ensure access to membrane-bound stem cell factor, HSCs require direct contact with these cell types. We and others previously reported substantial overlap between Cxcl12 and LepR cells.[26,29] We have now shown a proportion of HSCs locating within 5 μm of MKs, confirming previous results.[14,15] Mechanistically, MKs inhibit HSC proliferation through secreted proteins, including Tgfb1[15] and Cxcl4[14]; therefore, direct contact may not be required.

We identified BM populations with limited physical association with HSCs. Fewer than 6% of femoral and 10% of sternal HSCs locate near bone, compared with almost 20% reported earlier.[18] Similarly, <6% of HSCs were adjacent to Sca1$^+$ arteriolar cells, in agreement with a previous study,[13] but almost twofold lower than that in another study.[18] Consequently, HSCs do not preferentially locate close to NG2$^+$ periarteriolar cells, suggesting

that reported effects on HSC function[18] are mediated by secreted factors, as previously described.[31] We found almost no spatial association of HSCs with GFAP$^+$ Schwann cells, mainly located around Sca1$^+$ diaphyseal arteries.[26] Despite lacking physical association, the importance of those BM populations as functional homeostatic niches stands, but is most likely mediated by secreted factors. Finally, most HSCs did not associate with adipocytes. Importantly, HSC localization was conserved between both femurs and sterna, despite micro-anatomical differences. Notably, the hematopoietic cell type imaged is pivotal, because populations mainly consisting of multipotent progenitors (cKit$^+$Sca1$^+$ lineage) locate closer to the bone matrix and GFAP$^+$ Schwann cells, in a random and nonrandom fashion, respectively.[23]

Although we found HSCs close to the cell types described herein, our analyses revealed that the localization of HSC$^{\alpha\text{-cat}}$s reflected the cellular abundance of those BM populations, suggesting that HSC localization is mostly determined by microanatomical BM properties, rather than being actively selected by HSCs. Femoral HSC localization from sinusoids and bone in a recently developed HSC reporter mouse further confirmed this observation.[24] Furthermore, the frequency with which HSCs were found within specific niches correlated with the abundance of those niches. A large number of anatomical microenvironments were vacant during homeostasis and thus were not a limiting factor, a result that was further supported by recent findings that transplanting a high number of HSCs into non-conditioned recipients results in their successful long-term engraftment, without replacing host HSCs.[32] Empty niches may lack additional cell types or function under inflammation or stress. Alternatively, occupied niches may consist of currently unexplored subsets of sinusoidal, perisinusoidal, or stromal cells reflecting the recently reported heterogeneity of those populations[33,34] or being induced by HSCs themselves.[35,36] HSCs may modulate the gene and protein expression profile of specific BM cell types, making them functional niche cells only after interacting with HSCs. Such an HSC-niche unit is established only in the presence of both cell types, explaining why the number of potential niches vastly exceeds that of HSCs. This observation is in line with those in a previous study reporting differential transcriptional profiles of osteolineage cells, depending on their proximity to HSCs in situ.[37] Furthermore, it is well accepted that tumor cells can reprogram their microenvironment to favor disease progression,[34,38,39] most likely by hijacking the cross-talk mechanism between normal HSCs and their niche.[40]

The existence of distinct niches supporting HSCs with different divisional histories has also been debated. Previous studies using Ki67 as a proliferation marker not only led to contradictory results,[13,18] but were limited to a static view of the cell-cycle status providing no information on the divisional history of HSCs. We therefore used DOX-treated, double-transgenic SCL-tTA;H2B-GFP mice[19] to identify dormant (long-term

quiescent) HSPCs compared with age-matched H2B-GFP controls.[28] The advantage of endogenous labeling over 5-ethynyl-2'-deoxyuridine assays is the reliable marking of most immunophenotypic HSCs,[19] whereas a 150-day-long chase allows for efficient exclusion of labeled hematopoietic progenitors otherwise included in shorter chase periods.[19,41] Herein, we report that femoral and sternal dormant and nondormant adult HSPCs shared identical BM localization signatures, suggesting that functional differences between those subtypes may be niche independent and reflect intrinsic predetermined programs. This observation is in agreement with previous studies reporting identical behavior of clonally related adult HSCs in lineage contribution and repopulation kinetics after serial transplantations.[42-44] We do not exclude the possibility that other (ie, lineage-biased) adult HSC types have different niche signatures,[45] or that the same niches affect other hematopoietic cell types differently, such as instructing lymphoid progenitors[46] or inducing niche signature changes during aging and stress.[41] In line with these possibilities, we report that juvenile preswitch BM HSCs had a distinct BM localization signature: they preferentially associated with Cxcl12 stroma, potentially reflecting recently reported transcriptional differences between juvenile and adult Cxcl12 stroma cells.[47] They also located farther from sinusoids and MKs (33% of adult vs 15% of preswitch HSCs were close to both types simultaneously), in line with a possible inhibitory effect of MKs on HSC proliferation.[14,15] Further studies are needed to validate the functional relevance of those localization differences in juvenile HSCs.

Our study is based on mouse reporters yielding HSCs of a purity obtained by the latest purification methods. Approximately half of these cells failed to be classified as long-term, self-renewing HSCs in transplantation experiments, the current standard for assessing HSC function, despite increasing concerns about its accuracy in enumerating stem cell potential and reflecting unperturbed hematopoiesis.[48] It thus is possible that actual distribution of pure HSCs may deviate from those reported previously and in this study. However, our finding that dormant and nondormant cells have statistically indistinguishable distance distributions from all the studied niches does not support this possibility.

The quantification of 152 full-bone sections of different bone types and the 3 different HSC reporter systems used in this study help resolve existing confusion regarding the physical association of HSCs with putative BM-niche cells and the possible mechanisms of interaction (cell adhesion molecules or secreted factors) at tissue-wide level and single-cell resolution.

Authorship

Contribution: K.D.K. conceived the project, planned and performed all the experiments, analyzed the data, and wrote the manuscript with T.S.; L.K. programmed the script for estimating the number of available niches, with input from K.D.K.; N.C.-W., S.R., and A.T. performed the label-retaining experiments and provided bones from the SCL-tTA, H2B-GFP, and SCL-tTA;H2BGFP double-transgenic mice; C.C. and F.C. developed and provided bones from the Mds1[GFP/+]Flt3[Cre] reporter mouse; D.T.S. funded and supervised the project; T.S. funded, planned, and supervised the project; and all authors read and commented on the manuscript.

Conflict-of-interest disclosure: D.T.S. is a director and equity holder of Agios Pharmaceuticals, Magenta Therapeutics, Editas Medicines, ClearCreekBio, and Life-VaultBio; a founder of Fate Therapeutics and Magenta Therapeutics; and a consultant to FOG Pharma and VCanBio. The remaining authors declare no competing financial interests.

ORCID profiles: K.D.K., 0000-0002-9952-3463; L.K., 0000-0001-7332-3343; F.C., 0000-0002-5630-5909; A.T., 0000-0002-6212-3466; D.T.S., 0000-0001-9821-7133; T.S., 0000-0001-9320-0252.

Correspondence: Konstantinos D. Kokkaliaris, Department of Biosystems Science and Engineering, ETH Zurich, Mattenstrasse 26, 4058 Basel, Switzerland, e-mail: kkokkaliaris@mgh.harvard.edu; and Timm Schroeder, Department of Biosystems Science and Engineering, ETH Zurich, Mattenstrasse 26, 4058 Basel, Switzerland; e-mail: timm.schroeder@bsse.ethz.ch.

REFERENCES

1. Wilson A, Trumpp A. Bone-marrow haematopoietic-stem-cell niches. *Nat Rev Immunol.* 2006;6(2):93-106.

2. Mendelson A, Frenette PS. Hematopoietic stem cell niche maintenance during homeostasis and regeneration. *Nat Med.* 2014;20(8):833-846.

3. Morrison SJ, Scadden DT. The bone marrow niche for haematopoietic stem cells. *Nature.* 2014;505(7483):327-334.

4. Schofield R. The relationship between the spleen colony-forming cell and the haemopoietic stem cell. *Blood Cells.* 1978;4(1-2):7-25.

5. Pinho S, Frenette PS. Haematopoietic stem cell activity and interactions with the niche. *Nat Rev Mol Cell Biol.* 2019;20(5):303-320.

6. Kokkaliaris KD. Dissecting the spatial bone marrow microenvironment of hematopoietic stem cells. *Curr Opin Oncol.* 2020;32(2):154-161.

7. Zhang J, Niu C, Ye L, et al. Identification of the haematopoietic stem cell niche and control of the niche size. *Nature.* 2003;425(6960):836-841.

8. Calvi LM, Adams GB, Weibrecht KW, et al. Osteoblastic cells regulate the haematopoietic stem cell niche. *Nature.* 2003;425(6960):841-846.

9. Arai F, Hirao A, Ohmura M, et al. Tie2/angiopoietin-1 signaling regulates hematopoietic stem cell quiescence in the bone marrow niche. *Cell.* 2004;118(2):149-161.

10. Yamazaki S, Ema H, Karlsson G, et al. Nonmyelinating Schwann cells maintain hematopoietic stem cell hibernation in the bone marrow niche. *Cell*. 2011;147(5):1146-1158.

11. Méndez-Ferrer S, Michurina TV, Ferraro F, et al. Mesenchymal and haematopoietic stem cells form a unique bone marrow niche. *Nature*. 2010;466(7308):829-834.

12. Sugiyama T, Kohara H, Noda M, Nagasawa T. Maintenance of the hematopoietic stem cell pool by CXCL12-CXCR4 chemokine signaling in bone marrow stromal cell niches. *Immunity*. 2006;25(6):977-988.

13. Acar M, Kocherlakota KS, Murphy MM, et al. Deep imaging of bone marrow shows non-dividing stem cells are mainly perisinusoidal. *Nature*. 2015;526(7571):126-130.

14. Bruns I, Lucas D, Pinho S, et al. Megakaryocytes regulate hematopoietic stem cell quiescence through CXCL4 secretion. *Nat Med*. 2014;20(11):1315-1320.

15. Zhao M, Perry JM, Marshall H, et al. Megakaryocytes maintain homeostatic quiescence and promote post-injury regeneration of hematopoietic stem cells. *Nat Med*. 2014; 20(11):1321-1326.

16. Nakamura-Ishizu A, Takubo K, Kobayashi H, Suzuki-Inoue K, Suda T. CLEC-2 in megakaryocytes is critical for maintenance of hematopoietic stem cells in the bone marrow [published correction appears in *J Exp Med*. 2015;212(13):2323]. *J Exp Med*. 2015;212(12): 2133-2146.

17. Chen JY, Miyanishi M, Wang SK, et al. Hoxb5 marks long-term hematopoietic stem cells and reveals a homogenous perivascular niche. *Nature*. 2016;530(7589):223-227.

18. Kunisaki Y, Bruns I, Scheiermann C, et al. Arteriolar niches maintain haematopoietic stem cell quiescence. *Nature*. 2013; 502(7473):637-643.

19. Wilson A, Laurenti E, Oser G, et al. Hematopoietic stem cells reversibly switch from dormancy to self-renewal during homeostasis and repair [published correction appears in *Cell*. 2009;138(1):209]. *Cell*. 2008; 135(6):1118-1129.

20. Bernitz JM, Kim HS, MacArthur B, Sieburg H, Moore K. Hematopoietic Stem Cells Count and Remember Self-Renewal Divisions. *Cell*. 2016;167(5):1296-1309.e10.

21. Qiu J, Papatsenko D, Niu X, Schaniel C, Moore K. Divisional history and hematopoietic stem cell function during homeostasis. *Stem Cell Reports*. 2014;2(4):473-490.

22. Bowie MB, Kent DG, Dykstra B, et al. Identification of a new intrinsically timed developmental checkpoint that reprograms key hematopoietic stem cell properties. *Proc Natl Acad Sci USA*. 2007;104(14):5878-5882.

23. Coutu DL, Kokkaliaris KD, Kunz L, Schroeder T. Multicolor quantitative confocal imaging cytometry. *Nat Methods*. 2018;15(1):39-46.

24. Christodoulou C, Spencer JA, Yeh SA, et al. Live-animal imaging of native haematopoietic stem and progenitor cells. *Nature*. 2020; 578(7794):278-283.

25. Ding L, Morrison SJ. Haematopoietic stem cells and early lymphoid progenitors occupy distinct bone marrow niches [published correction appears in *Nature*. 2014;514(7521): 262]. *Nature*. 2013;495(7440):231-235.

26. Coutu DL, Kokkaliaris KD, Kunz L, Schroeder T. Three-dimensional map of non-hematopoietic bone and bone-marrow cells and molecules. *Nat Biotechnol*. 2017;35(12): 1202-1210.

27. van der Wath RC, Wilson A, Laurenti E, Trumpp A, Liò P. Estimating dormant and active hematopoietic stem cell kinetics through extensive modeling of bromodeoxyuridine label-retaining cell dynamics. *PLoS One*. 2009;4(9):e6972.

28. Morcos MNF, Zerjatke T, Glauche I, et al. Continuous mitotic activity of primitive hematopoietic stem cells in adult mice. *J Exp Med*. 2020;217(6):e20191284.

29. Ding L, Saunders TL, Enikolopov G, Morrison SJ. Endothelial and perivascular cells maintain haematopoietic stem cells. *Nature*. 2012; 481(7382):457-462.

30. Barker JE. Sl/Sld hematopoietic progenitors are deficient in situ. *Exp Hematol*. 1994;22(2): 174-177.

31. Asada N, Kunisaki Y, Pierce H, et al. Differential cytokine contributions of perivascular haematopoietic stem cell niches. *Nat Cell Biol*. 2017;19(3):214-223.

32. Shimoto M, Sugiyama T, Nagasawa T. Numerous niches for hematopoietic stem cells remain empty during homeostasis. *Blood*. 2017;129(15):2124-2131.

33. Tikhonova AN, Dolgalev I, Hu H, et al. The bone marrow microenvironment at single-cell resolution. *Nature*. 2019;569(7755):222-228.

34. Baryawno N, Przybylski D, Kowalczyk MS, et al. A Cellular Taxonomy of the Bone Marrow Stroma in Homeostasis and Leukemia. *Cell*. 2019;177(7):1915-1932.e16.

35. Mercier FE, Ragu C, Scadden DT. The bone marrow at the crossroads of blood and immunity. *Nat Rev Immunol*. 2011;12(1):49-60.

36. Zhou BO, Ding L, Morrison SJ. Hematopoietic stem and progenitor cells regulate the regeneration of their niche by secreting Angiopoietin-1. *eLife*. 2015;4:e05521.

37. Silberstein L, Goncalves KA, Kharchenko PV, et al. Proximity-Based Differential Single-Cell Analysis of the Niche to Identify Stem/Progenitor Cell Regulators. *Cell Stem Cell*. 2016; 19(4):530-543.

38. Medyouf H, Mossner M, Jann JC, et al. Myelodysplastic cells in patients reprogram mesenchymal stromal cells to establish a transplantable stem cell niche disease unit. *Cell Stem Cell*. 2014;14(6):824-837.

39. Schepers K, Campbell TB, Passegué E. Normal and leukemic stem cell niches: insights and therapeutic opportunities. *Cell Stem Cell*. 2015;16(3):254-267.

40. Hanahan D, Weinberg RA. Hallmarks of cancer: the next generation. *Cell*. 2011;144(5): 646-674.

41. Saçma M, Pospiech J, Bogeska R, et al. Haematopoietic stem cells in perisinusoidal niches are protected from ageing. *Nat Cell Biol*. 2019;21(11):1309-1320.

42. Müller-Sieburg CE, Cho RH, Thoman M, Adkins B, Sieburg HB. Deterministic regulation of hematopoietic stem cell self-renewal and differentiation. *Blood*. 2002;100(4): 1302-1309.

43. Yu VWC, Yusuf RZ, Oki T, et al. Epigenetic Memory Underlies Cell-Autonomous Heterogeneous Behavior of Hematopoietic Stem Cells [published correction appears in *Cell*. 2017;168(5):944-945.]. *Cell*. 2016;167(5): 1310-1322.e17.

44. Baryawno N, Severe N, Scadden DT. Hematopoiesis: Reconciling Historic Controversies about the Niche. *Cell Stem Cell*. 2017; 20(5):590-592.

45. Pinho S, Marchand T, Yang E, Wei Q, Nerlov C, Frenette PS. Lineage-Biased Hematopoietic Stem Cells Are Regulated by Distinct Niches. *Dev Cell*. 2018;44(5):634-641.e4.

46. Cordeiro Gomes A, Hara T, Lim VY, et al. Hematopoietic Stem Cell Niches Produce Lineage-Instructive Signals to Control Multipotent Progenitor Differentiation. *Immunity*. 2016;45(6):1219-1231.

47. Helbling PM, Piñeiro-Yáñez E, Gerosa R, et al. Global Transcriptomic Profiling of the Bone Marrow Stromal Microenvironment during Postnatal Development, Aging, and Inflammation. *Cell Rep*. 2019;29(10): 3313-3330.e4.

48. Busch K, Rodewald HR. Unperturbed vs. posttransplantation hematopoiesis: both in vivo but different. *Curr Opin Hematol*. 2016;23(4): 295-303.